ACS APPLIED MATERIALS & INTERFACES

www.acsami.org Research Article

Type-II Interface Band Alignment in the vdW PbI_2−$MoSe_2$ Heterostructure

Junting Xiao, Lei Zhang, Hui Zhou, Ziyi Shao, Jinxin Liu, Yuan Zhao, Youzhen Li, Xiaoliang Liu, Haipeng Xie, Yongli Gao, Jia-Tao Sun,* Andrew T. S. Wee,* and Han Huang*

Cite This: *ACS Appl. Mater. Interfaces* 2020, 12, 32099−32105 Read Online

ACCESS | Metrics & More | Article Recommendations | Supporting Information

ABSTRACT: Energy band alignments at heterostructure interfaces play key roles in device performance, especially between two-dimensional atomically thin materials. Herein, van der Waals PbI_2−$MoSe_2$ heterostructures fabricated by *in situ* PbI_2 deposition on monolayer $MoSe_2$ are comprehensively studied using scanning tunneling microscopy/spectroscopy, atomic force microscopy, photoemission spectroscopy, and Raman and photoluminescence (PL) spectroscopy. PbI_2 grows on $MoSe_2$ in a quasi layer-by-layer epitaxial mode. A type-II interface band alignment is proposed between PbI_2 and $MoSe_2$ with the conduction band minimum (valence band maximum) located at PbI_2 ($MoSe_2$), which is confirmed by first-principles calculations and the existence of interfacial excitons revealed using temperature-dependent PL. Our findings provide a scalable method to fabricate PbI_2−$MoSe_2$ heterostructures and new insights into the electronic structures for future device design.

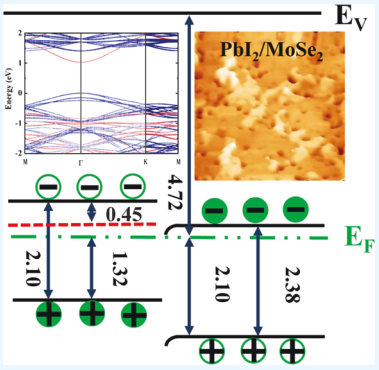

KEYWORDS: *PbI_2, $MoSe_2$, vdW heterostructure, type II band alignment, Raman and PL spectroscopy*

INTRODUCTION

Progress on van der Waals (vdW) heterostructures made of atomically thin transition metal dichalcogenides (TMDCs) has offered new electronic and optoelectronic applications, where energy band alignments at interfaces play key roles.[1−4] Type-II band alignment (staggered gap) has extensive applications in photovoltaics and optoelectronics, attributed to the enhanced abilities of the photogenerated charge carriers to cross the interface because of the built-in electric field.[5−7] In contrast, type-I and type-III (straddling gap and broken gap) band alignments are used for light-emitting and tunneling field effect transistors, respectively.[8,9] Fabrication of vdW heterostructures with atomically and electronically sharp interfaces plays key roles in essential studies and applications.

Layered lead iodide (PbI_2) is a strong light adsorption and emission material, being widely used in lead halide perovskites[10−12] and having good potential in optoelectronic applications.[13] For instance, millimeter-sized freestanding PbI_2 flakes can be transferred and stacked on a single crystal antimony sulphoiodide whisker to form a high-performance 2D-1D vdW heterostructure photodetector.[14] The 2D vdW heterostructure of PbI_2 and graphene is applicable to flexible or stretchable electronics.[15] PbI_2 shows a transition from the direct band gap to indirect one when reduced to one monolayer,[16] while the reverse is true for TMDCs such as MoS_2, $MoSe_2$, and $MoTe_2$. For PbI_2−TMDC vdW heterostructures, energy band alignments have been investigated recently using the PL method. The PbI_2−WS_2 heterostructure, which is fabricated by a dry method to stack the exfoliated monolayer WS_2 on top of the multilayer PbI_2 single crystal flakes synthesized in solution, shows a type-II band alignment, whereas PbI_2−MoS_2 fabricated in the same method exhibits a type-I band alignment.[17] On the contrary, the PbI_2−MoS_2 heterojunction *via* thermal deposition displays a type-II band alignment,[18] in line with recent theoretical prediction.[19] The two-step CVD-grown PbI_2−WS_2 and PbI_2−WSe_2 heterobilayers show a type-I and type-II band alignment, respectively.[20] Therefore, more research studies in this field are called for. Most heterostructures studied have been based on small micrometer-scale flakes using transfer technology. High quality and scalable production without transfer are required for commercial applications.

Molecular beam epitaxy (MBE) is the method of choice to prepare high-quality large-area monolayer $MoSe_2$,[21] a promising semiconductor with a high mobility of over 120 $cm^2\ V^{-1}\ s^{-1}$ for (flexible) transistors.[22,23] Herein, PbI_2 thin films were thermally deposited onto MBE-grown monolayer $MoSe_2$ under high-vacuum conditions to fabricate PbI_2−$MoSe_2$ vdW heterostructures. Scanning tunneling microscopy/spectroscopy

Received: March 17, 2020
Accepted: June 17, 2020
Published: June 17, 2020

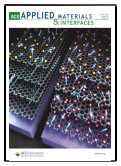

https://dx.doi.org/10.1021/acsami.0c04985
ACS Appl. Mater. Interfaces 2020, 12, 32099−32105

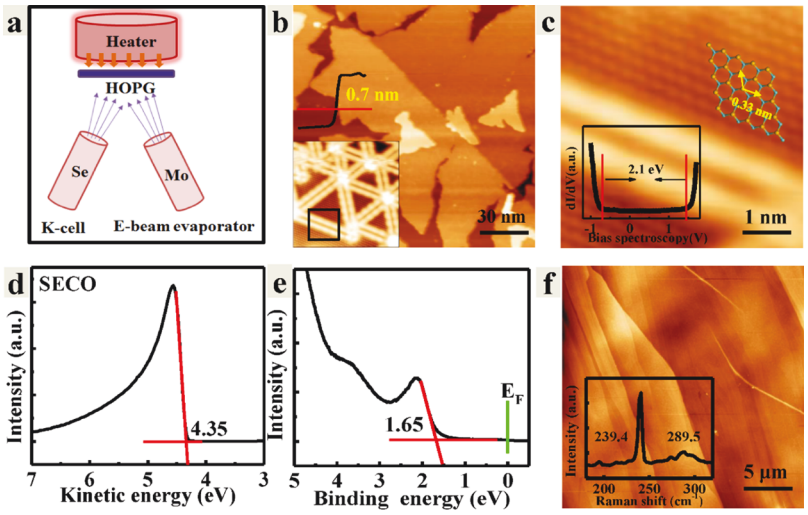

Figure 1. Characterization of the MBE-grown monolayer $MoSe_2$ on HOPG. (a) Schematic of the MBE growth of $MoSe_2$. (b) Large-scale STM image (U_{tip} = −3.78 V, I = 10 pA). The line profile shows a height of 0.7 nm. The inset zoom-in STM image shows the typical wagon-wheel patterns of $MoSe_2$ (size: 15 × 15 nm^2; U_{tip} = −1.3 V, I = 122 pA). (c) Atomic-resolution STM image (U_{tip} = −1.3 V, I = 122 pA) overlapped by a ball-and-stick model, showing a lattice constant of ∼0.33 nm. Se (Mo) atoms are shown in orange (green). The inserted STS spectrum (U_{tip} = −0.7 V, I = 50 pA) reveals a band gap of ∼2.1 eV. (d,e) SECO and valence band structure, respectively. (f) AFM image showing an atomically smooth surface. Inset: typical Raman spectrum.

(STM/STS), atomic force microscopy (AFM), photoemission spectroscopy (PES), and Raman and photoluminescence (PL) spectroscopy measurements were conducted to investigate them. AFM results disclose the layered structure of PbI_2 on $MoSe_2$. Raman and XPS results reveal the stability of $MoSe_2$ and PbI_2−$MoSe_2$ heterostructures in air. Ultraviolet photoelectron spectroscopy results reveal that a type-II energy band alignment in vertical PbI_2−$MoSe_2$ vdW heterostructures is formed. First-principles calculations and PL measurements further confirm the type-II band alignment.

METHODS

Sample Preparation. MBE-grown monolayer $MoSe_2$ samples were prepared on HOPG substrates in an ultrahigh vacuum (UHV) chamber with a base pressure of ∼1 × 10^{-9} mbar,[24,25] as illustrated in Figure 1a. Se (Sigma, 99.999%) was evaporated from a K-cell at 470 K, while Mo (ESPI Metals, 99.999%) was evaporated from an e-beam evaporator. To ensure sufficient Se atoms to react with Mo, the HOPG substrate was held at a temperature of 620 K under Se-rich conditions. Following MBE growth, the sample was capped with a ∼15 nm-thick Se layer. For subsequent STM/STS and PES characterization and PbI_2 deposition, the capped sample was annealed at 520 K for 2 h for the purpose of complete removal of the Se capping layer. Atomically thin $MoSe_2$ flakes were mechanically exfoliated from the bulk crystals (Shanghai Onway Technology Co., Ltd) onto 300 nm SiO_2/Si substrates using the Scotch tape method.[26] Their thicknesses were identified by optical microscopy (OM) and Raman spectroscopy.[27] Sublimation-purified PbI_2 (Aldrich, 98+ %) was evaporated from a K-cell in an high vacuum chamber with a base pressure of 1.0 × 10^{-7} mbar, where a quartz microbalance is equipped to monitor the deposited PbI_2 film thickness.[18,28] The nominal deposition rate of PbI_2 was calibrated to be 1.0 nm/min at a deposition temperature of ∼600 K.

Measurements. STM/STS measurements were carried out at 77 K in a custom-built multichamber UHV system housing an Omicron LT-STM instrument with a base pressure better than 6.0 × 10^{-11} mbar in the surface science laboratory at the NUS.[24] STM images were acquired in the constant current mode and bias voltages were applied to the tip. PES measurements were implemented in a spectrometer chamber (base pressure: 2.0 × 10^{-10} mbar) equipped with a SPECS PHOIBOS150 hemispherical energy analyzer, a monochromatic SPECS XR-MF X-ray source (Al Kα, $h\nu$ = 1486.7 eV), and a SPECS microwave UV light source (He Iα, $h\nu$ = 21.2 eV).[29,30] Raman and PL measurements were performed in an inVia Qontor system (Renishaw, UK) using a 532 nm laser with a spot size less than 1 μm and a 1800 lines/mm grating.[31] OM measurements were carried out in a CaiKang DMM-200C optical microscope. AFM images were captured with a 5500 SPM system (Agilent, USA) in the tapping mode.[32] Except for STM/STS measurements at liquid nitrogen temperature (77 K), all other measurements were performed at RT.

Density Functional Theory Calculations. The first-principles calculations based on density functional theory were performed with Vienna Ab initio Simulation Package (VASP)[33,34] The projector-augmented wave pseudopotential and Perdew−Burke−Ernzerhof exchange−correlation functional were used. The energy cutoff of the plane-wave basis was set as 400 eV.[35,36] The vacuum thickness was set to be larger than 15 Å. For the heterostructure, a 2 × 2 lattice of the PbI_2 monolayer is placed on a 3 × 3 lattice of the $MoSe_2$ monolayer. The first Brillouin Zone (BZ) was sampled with a gamma-centered k-mesh. A 6 × 6 × 1 k-mesh is used for structural optimization and self-consistent calculations because of the larger supercell. To determine the partial occupancies for each orbital, Gaussian smearing with a width of 0.05 eV was used. The convergence of the force on each atom to optimize their positions was less than 0.01 eV/Å. The convergence condition of the electronic self-consistent loop was 10^{-5} eV. Additionally, spin−orbit coupling (SOC) was included in the electronic self-consistent loop and band structure calculation.[37]

RESULTS AND DISCUSSIONS

The representative large-scale STM image in Figure 1b shows that the as-grown $MoSe_2$ flakes appear as leaf-like islands on HOPG with a height of ∼0.7 nm (line profile), indicating its monolayer thickness. A few bilayer islands form because of kinetic causation during MBE growth.[38] The inserted zoom-in STM image shows wagon-wheel patterns formed by mirror twin boundaries (MTBs), which are ascribed to the one-dimensional Se defects.[39] Figure 1c shows an atomic-resolution STM image of the black square region in panel b. The atomic features with a lattice constant of 0.33 nm are assigned as the upper-layer Se atoms in the hexagonal lattice of $MoSe_2$. To

https://dx.doi.org/10.1021/acsami.0c04985
ACS Appl. Mater. Interfaces 2020, 12, 32099−32105

guide the eye, a piece of the ball-and-stick lattice model is overlapped with Se (Mo) atoms in orange (green). The inserted STS spectrum obtained in the region away from MTBs reveals an energy band gap of ∼2.10 eV, consistent with previous reports.[40,41] The valence band maximum (VBM) and conduction band minimum (CBM) are located at 1.45 and −0.65 eV, respectively, suggesting its n-type semiconducting nature. This can be attributed to intrinsic point defects such as vacancies or lattice antisites and doping from the underlying substrate.[42] Because of the additional nonradiative channels that are opened by the highly-conductive HOPG substrate which both reduces the overall PL signal and the quasiparticle lifetime,[41] no band-edge PL emissions of $MoSe_2$/HOPG were detected, in consistence with previous report.[38] In contrast, an optical band gap of 1.57 eV is detected under the same experimental presetting conditions on mechanically exfoliated monolayer $MoSe_2$ flakes (*cf.* Figure 5).

The secondary electron cutoff (SECO) of monolayer $MoSe_2$ on HOPG (Figure 1d) reveals a work function (WF) of ∼4.35 eV. The VBM of $MoSe_2$ (Figure 1e) is measured to be ∼1.65 eV below the Fermi level (E_F), confirming its n-type semiconducting nature, consistent with our STS results. Measurements in air were also performed after Se capping layer removal to confirm the high quality and ambient stability of $MoSe_2$. The corresponding AFM image in Figure 1f shows the atomically smooth surface. In contrast, the AFM image of as-received $MoSe_2$ in Figure S1a shows randomly distributed protrusions. The corresponding Mo 3d and Se 3d core level XPS spectra (Figure S1b,c) confirm that the Se capping layer has desorbed thoroughly. The typical Raman spectrum in Figure 1f clearly shows two characteristic peaks at 239.4 and 289.5 cm^{-1}, which arise from the out-of-plane vibration mode of Se atoms (A_{1g}) and in-plane vibration of Mo and Se atoms (E^1_{2g}), respectively.[43,44] As shown in Figure S2, the full width at half maximum of the A_{1g} peak of MBE-grown monolayer $MoSe_2$ (4.2 cm^{-1}) is similar to that of exfoliated monolayer $MoSe_2$ (3.9 cm^{-1}), verifying their same high quality.

Upon nominal 3 nm-thick PbI_2 deposition, the samples were *ex situ*-characterized using AFM, Raman, XPS, and PL. The typical AFM image (Figure 2a) shows similar terrace features as in Figure 1f but rougher. This suggests that at RT, the vdW epitaxial growth of PbI_2 on $MoSe_2$ is not as perfect as that on MoS_2.[18] A typical zoomed-in AFM image in Figure 2b and the profile (insert) show that single-layered islands with smooth surfaces start to grow on the uncompleted PbI_2 layers, indicating a quasi layer-by-layer vdW epitaxial growth mode of PbI_2 on $MoSe_2$ at RT. The Raman spectrum in Figure 2a inset shows both the $MoSe_2$-related and PbI_2-related peaks. The $MoSe_2$-related characteristic peak A_{1g} blue-shifts by 0.2 to 239.6 cm^{-1} and E^1_{2g} red-shifts by 0.4 to 289.1 cm^{-1}. The A_{1g} frequency increases with layer numbers mainly because of the enlarged interlayer interaction, while the E^1_{2g} frequency decreases because of the increased dielectric screening and the reduced overall restoring force on the atoms.[45−48] The first possible reason for the abovementioned shift is that the deposited PbI_2 caused interlayer coupling. Second, A_{1g} is sensitive to electron−phonon coupling at the interface, while E^1_{2g} is sensitive to the built-in strain.[49] The P-doping can lead E^1_{2g} and A_{1g} modes red- and blue-shift, respectively.[50] A second possible reason is the interfacial charge transfer from $MoSe_2$ to PbI_2. PbI_2-related Raman peaks located at 70.1, 94.1, and 108.1 cm^{-1} are identified to the in-plane E_g, the out-of-plane A_{1g}, and the infrared-active A_{2u} modes, respectively.[51]

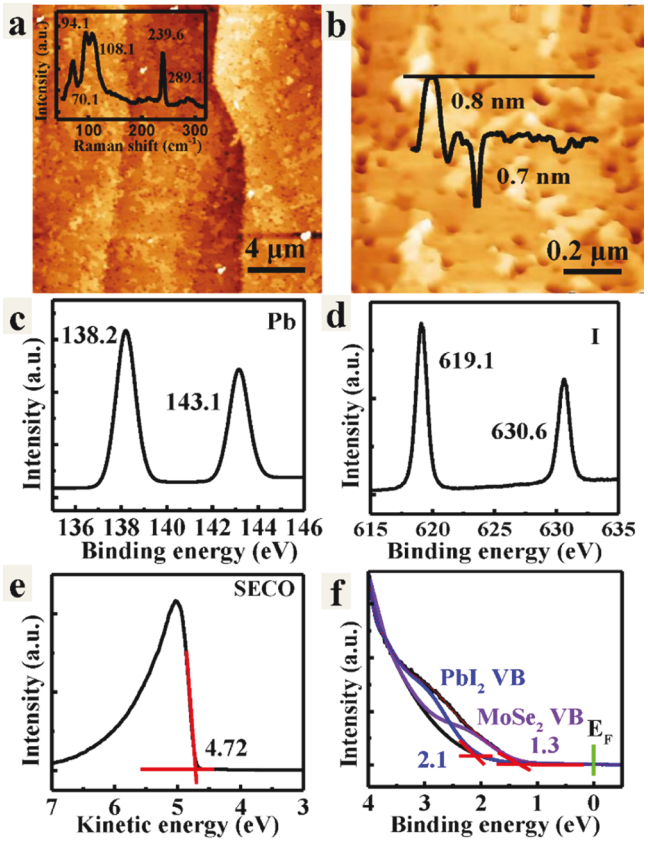

Figure 2. Characterization of the 3 nm-thick PbI_2−$MoSe_2$ vdW heterostructure. (a) Typical AFM image showing similar terrace features as the clean sample but rougher. The inserted Raman spectrum confirms the presence of PbI_2 and $MoSe_2$. (b) Amplified 3D AFM image and profile indicating a quasi layer-by-layer growth mode of PbI_2 on $MoSe_2$. (c,d) Pb 4f and I 3d core level XPS spectra, respectively. (e,f) SECO and valance band structure, respectively.

To further understand the chemical states of PbI_2, high-resolution XPS spectra of Pb 4f and I 3d were collected (Figure 2c,d, respectively). The peaks at 138.2 and 143.1 eV (619.1 and 630.6 eV) are assigned to Pb $4f_{7/2}$ and Pb $4f_{5/2}$ (I $3d_{5/2}$ and I $3d_{3/2}$), respectively. The Pb/I ratio is calculated to be 1:1.9. The WF is measured to be 4.72 eV (Figure 2e) and the VBM is at ∼1.32 eV below E_F (Figure 2f). This is inconsistent with our previous report that vapor-grown PbI_2 is heavily n-doped.[18] Because of the higher WF of PbI_2−$MoSe_2$ (4.72 eV) than that of $MoSe_2$ (4.35 eV), electron transfer from $MoSe_2$ to PbI_2 is expected at the interface, causing PbI_2 to be further n-doped. Thus, the VBM of $MoSe_2$ (PbI_2) will shift upward (downward). Because of the semimetallic nature of HOPG and the monolayer thickness of $MoSe_2$, no bending but a rigid shift of the $MoSe_2$ energy bands is expected upon PbI_2 deposition. Thus, we assign the band onset at 1.32 eV to the VBM of $MoSe_2$ rather than to that of PbI_2. Figure 2f shows a second peak centered at ∼2.6 eV below E_F, similar to our previous report.[18] The onset of this band located at 2.1 ± 0.1 eV is assigned to the VBM of PbI_2.

According to the abovementioned results, the energy band diagrams of $MoSe_2$ and PbI_2−$MoSe_2$ are proposed in Figure 3a,b, respectively. MBE-grown $MoSe_2$ on HOPG is an n-type semiconductor with the VBM at 1.65 eV below E_F. Upon PbI_2 deposition, the VBM of monolayer $MoSe_2$ shifts rigidly to 1.32 eV because of electron transfer to PbI_2. For the same reason,

https://dx.doi.org/10.1021/acsami.0c04985
ACS Appl. Mater. Interfaces 2020, 12, 32099−32105

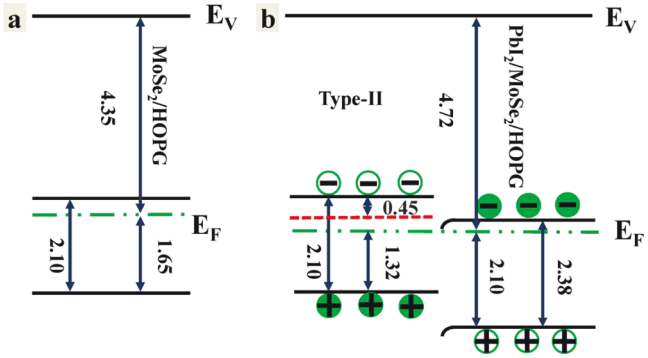

Figure 3. Energy band diagrams of $MoSe_2$ before (a) and after (b) PbI_2 deposition. The red-dashed line in (b) highlights the energy level of 1s exciton.

the bands of PbI_2 films bend downward at the interface. Such band bending will lower the VBM of PbI_2 films and enhance the band offset between $MoSe_2$ and PbI_2, as shown in Figure 3b. Thus, a type-II band alignment is formed at the interface. According to the previously reported PL peak of $MoSe_2$ on HOPG being at 1.65 ± 0.02 eV at liquid nitrogen temperature,[41,52] the $MoSe_2$ 1s exciton binding energy is calculated to be 0.45 ± 0.02 eV, highlighted by the red-dashed line in Figure 3b. The CBM of PbI_2 remains lower than the 1s exciton of $MoSe_2$, which is beneficial to the formation of interfacial exciton. Thus, photogenerated electrons in $MoSe_2$ will spontaneously transfer to the CBM of PbI_2, resulting in PL quenching of monolayer $MoSe_2$. To verify this hypothesis, first-principles calculations and PL measurements on PbI_2−$MoSe_2$ (exfoliated monolayer) were performed.

Figure 4 shows the first-principles calculated results. The in-plane lattice constants of $MoSe_2$ and PbI_2 are 3.33 and 4.69 Å, respectively. Both have hexagonal symmetry. To minimize the lattice mismatch between the stacked $MoSe_2$ and PbI_2, 2 × 2 PbI_2 cells and 3 × 3 $MoSe_2$ cells were adopted to build the supercell, whose overall lattice mismatch in PbI_2 and $MoSe_2$ lattices are 5.2 and 0.9%, respectively. The lattice constant of the heterostructure is closer to that of the 3 × 3 $MoSe_2$ cells. Figure 4a shows the side and top views of the PbI_2−$MoSe_2$ heterostructure. The separation between them is calculated to be 7.64 Å, confirming the vdW interfacial interaction. Figure 4b shows the corresponding projected band structure. The band gap is calculated to be 1.029 eV with both CBM and VBM at the Γ point, indicating a direct band gap. The blue and red bands are from $MoSe_2$ and PbI_2, respectively. The CBM and VBM of the PbI_2−$MoSe_2$ heterostructure are located at PbI_2 and $MoSe_2$, respectively, indicating a type-II band alignment. It is well-known that indirect to direct band gap transition occurs when the thickness of PbI_2 increases from monolayer to bulk. Our calculated results show that for thicker PbI_2 on monolayer $MoSe_2$, the band gap remains direct but slightly smaller. Figure S3 shows the calculated results for the heterostructure of four layers of PbI_2 and one layer of $MoSe_2$. The type-II band alignment is enhanced.

Figure 5 shows the Raman (a) and PL (b) spectra of exfoliated monolayer $MoSe_2$ flakes before and after 3 nm-thick

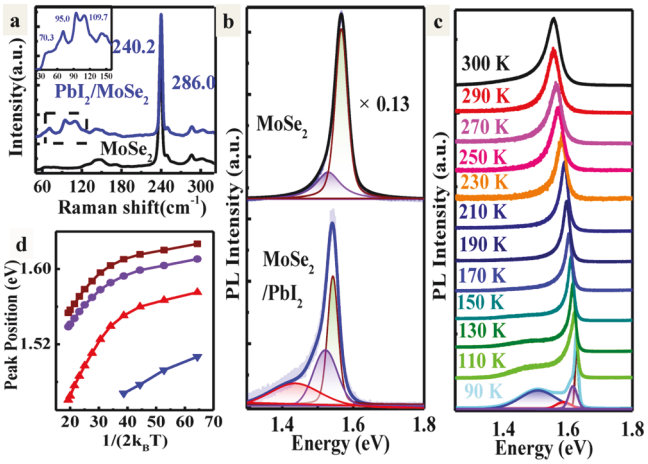

Figure 5. PbI_2 on exfoliated $MoSe_2$. (a) Raman and (b) PL spectra of monolayer $MoSe_2$ before and after PbI_2 deposition. (c) Temperature-dependent PL spectra of the PbI_2−$MoSe_2$ vdW heterostructure from 90 to 300 K. (d) Plotted PL peak position evolutions as a function of temperature.

PbI_2 deposition. The corresponding morphologies are shown in Figure S4. The Raman spectra show similar features as those in Figure 1f ($MoSe_2$) and Figure 2a (PbI_2−$MoSe_2$), confirming the formation of high quality PbI_2−$MoSe_2$ heterostructures. The upper panel in Figure 5b shows the PL spectrum of exfoliated monolayer $MoSe_2$ flakes, which can be fitted by two peaks at 1.57 (A^0) and 1.52 eV (A^-). Upon PbI_2 deposition, the emission intensity is obviously lowered to about one over seven of that of as-exfoliated $MoSe_2$ flakes, consistent with the above-discussed type-II interface band alignment. Furthermore, to fit the PL spectrum, one more peak is required at ∼1.43 eV, which is assigned to the interlayer excitons instead

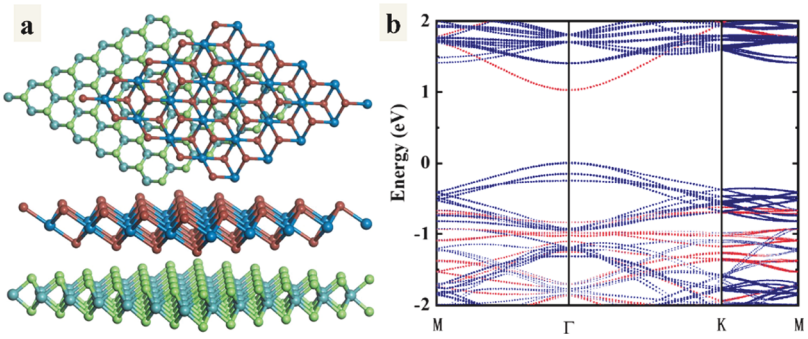

Figure 4. First-principles calculations on the PbI_2−$MoSe_2$ heterostructure. (a) Top and side views of the PbI_2−$MoSe_2$ heterostructure. (b) Calculated projected band structure of the PbI_2−$MoSe_2$ heterostructure with SOC. The bands plotted in blue and red are dominated by $MoSe_2$ and PbI_2, respectively.

https://dx.doi.org/10.1021/acsami.0c04985
ACS Appl. Mater. Interfaces 2020, 12, 32099−32105

of new tail states induced by PbI_2 or $MoSe_2$ below-gap states.[18] The corresponding optical band gap is consistent with that in our proposed energy band diagrams in Figure 3b. Figure 5c shows the temperature-dependent PL spectra of the PbI_2–$MoSe_2$ vdW heterostructure from 90 to 300 K. At 90 K, the defect-bounded exciton-related peak[53,54] is observed at 1.51 eV with a binding energy of 0.12 eV, which disappears at 150 K and above. The corresponding PL spectrum fitting details are shown in Figure S5. As shown in Figure 5d, all the intrinsic three peaks red-shift with the temperature increasing. According to conventional semiconductor theory,[55] it can be ascribed to the stronger electron–phonon interaction and the slight bonding length enlargement.[56] The standard semiconducting band gap model perfectly fits the dependence of all the intrinsic three peaks on temperature, as discussed in the Supporting Information.

■ CONCLUSIONS

In summary, we have systematically investigated the growth and electronic structures of PbI_2-monolayer $MoSe_2$ heterostructures. AFM results reveal a quasi layer-by-layer vdW epitaxial growth mode of PbI_2 on $MoSe_2$. A type-II energy band alignment at the interface of PbI_2–$MoSe_2$ is proposed and verified by first-principles calculations and the existence of interfacial excitons. The results of this work provide a deeper understanding of the vertical PbI_2–$MoSe_2$ heterostructure, which is important for future electronic device design.

■ ASSOCIATED CONTENT

Supporting Information

The Supporting Information is available free of charge at https://pubs.acs.org/doi/10.1021/acsami.0c04985.

As-received $MoSe_2$ before and after removing the Se capping layer, Results on exfoliated monolayer $MoSe_2$, Projected band structure of the heterostructure consists of four layers of PbI_2 and one layer of $MoSe_2$, and Fittings of PL peaks (PDF)

■ AUTHOR INFORMATION

Corresponding Authors

Han Huang − *Hunan Key Laboratory of Super-Microstructure and Ultrafast Process, School of Physics and Electronics, Central South University, Changsha 410083, P. R. China;* orcid.org/0000-0003-0641-1962; Email: physhh@csu.edu.cn

Jia-Tao Sun − *School of Information and Electronics, MIIT Key Laboratory for Low-Dimensional Quantum Structure and Devices, Beijing Institute of Technology, Beijing 100081, China; Institute of Physics, Chinese Academy of Sciences, Beijing 100190, China*; Email: jtsun@bit.edu.cn

Andrew T. S. Wee − *Department of Physics, National University of Singapore, 117542, Singapore;* orcid.org/0000-0002-5828-4312; Email: phyweets@nus.edu.sg

Authors

Junting Xiao − *Hunan Key Laboratory of Super-Microstructure and Ultrafast Process, School of Physics and Electronics, Central South University, Changsha 410083, P. R. China*

Lei Zhang − *Department of Physics, National University of Singapore, 117542, Singapore*

Hui Zhou − *Institute of Physics, Chinese Academy of Sciences, Beijing 100190, China*

Ziyi Shao − *Hunan Key Laboratory of Super-Microstructure and Ultrafast Process, School of Physics and Electronics, Central South University, Changsha 410083, P. R. China*

Jinxin Liu − *Hunan Key Laboratory of Super-Microstructure and Ultrafast Process, School of Physics and Electronics, Central South University, Changsha 410083, P. R. China*

Yuan Zhao − *Hunan Key Laboratory of Super-Microstructure and Ultrafast Process, School of Physics and Electronics, Central South University, Changsha 410083, P. R. China*

Youzhen Li − *Hunan Key Laboratory of Super-Microstructure and Ultrafast Process, School of Physics and Electronics, Central South University, Changsha 410083, P. R. China;* orcid.org/0000-0001-8994-3627

Xiaoliang Liu − *Hunan Key Laboratory of Super-Microstructure and Ultrafast Process, School of Physics and Electronics, Central South University, Changsha 410083, P. R. China*

Haipeng Xie − *Hunan Key Laboratory of Super-Microstructure and Ultrafast Process, School of Physics and Electronics, Central South University, Changsha 410083, P. R. China*

Yongli Gao − *Department of Physics and Astronomy, University of Rochester, Rochester, New York 14627, United States; Hunan Key Laboratory of Super-Microstructure and Ultrafast Process, School of Physics and Electronics, Central South University, Changsha 410083, P. R. China*

Complete contact information is available at: https://pubs.acs.org/10.1021/acsami.0c04985

Notes

The authors declare no competing financial interest.

■ ACKNOWLEDGMENTS

Discussion with Dr. Chen Shi at the University of Macao is greatly appreciated. We acknowledge the financial support from the National Natural Science Foundation (NSF) of China (grants nos. 11874427, 11774396, 11974045) and the National Key Research and Development Program of China (grants no. 2016YFA0202300). H.H. acknowledges support from the Innovation-Driven project of Central South University (grants no. 2017CX018) and from the Natural Science Foundation of Hunan province (grants no. 2016JJ1021). J.-T.S. acknowledges support from "Strategic Priority Research Program (B)" of CAS (grants no. XDB30000000) and Beijing Institute of Technology Research Fund Program for Young Scholars (grants no. 3050011181909).Y. G. acknowledges the support from National Science Foundation DMR-1903962. J. X. acknowledges the support from the Fundamental Research Funds for the Central Universities of Central South University (grants no. 2020zzts368).

■ REFERENCES

(1) Britnell, L.; Ribeiro, R. M.; Eckmann, A.; Jalil, R.; Belle, B. D.; Mishchenko, A.; Kim, Y. J.; Gorbachev, R. V.; Georgiou, T.; Morozov, S. V.; Grigorenko, A. N.; Geim, A. K.; Casiraghi, C.; Neto, A. H. C.; Novoselov, K. S. Strong Light-Matter Interactions in Heterostructures of Atomically Thin Films. *Science* **2013**, *340*, 1311−1314.

(2) Rivera, P.; Schaibley, J. R.; Jones, A. M.; Ross, J. S.; Wu, S.; Aivazian, G.; Klement, P.; Seyler, K.; Clark, G.; Ghimire, N. J.; Yan, J.; Mandrus, D. G.; Yao, W.; Xu, X. Observation of Long-Lived Interlayer Excitons in Monolayer $MoSe_2$–WSe_2 Heterostructures. *Nat. Commun.* **2015**, *6*, 6242.

(3) Huang, C.; Wu, S.; Sanchez, A. M.; Peters, J. J. P.; Beanland, R.; Ross, J. S.; Rivera, P.; Yao, W.; Cobden, D. H.; Xu, X. Lateral

Heterojunctions within Monolayer $MoSe_2$−WSe_2 Semiconductors. *Nat. Mater.* **2014**, *13*, 1096−1101.
(4) Hanbicki, A. T.; Chuang, H.-J.; Rosenberger, M. R.; Hellberg, C. S.; Sivaram, S. V.; McCreary, K. M.; Mazin, I. I.; Jonker, B. T. Double Indirect Interlayer Exciton in a $MoSe_2$/WSe_2 van Der Waals Heterostructure. *ACS Nano* **2018**, *12*, 4719−4726.
(5) Baranowski, M.; Surrente, A.; Klopotowski, L.; Urban, J. M.; Zhang, N.; Maude, D. K.; Wiwatowski, K.; Mackowski, S.; Kung, Y. C.; Dumcenco, D.; Kis, A.; Plochocka, P. Probing the Interlayer Exciton Physics in a MoS_2/$MoSe_2$/MoS_2 van Der Waals Heterostructure. *Nano Lett.* **2017**, *17*, 6360−6365.
(6) Zheng, X.; Wei, Y.; Liu, J.; Wang, S.; Shi, J.; Yang, H.; Peng, G.; Deng, C.; Luo, W.; Zhao, Y.; Li, Y.; Sun, K.; Wan, W.; Xie, H.; Gao, Y.; Zhang, X.; Huang, H. A Homogeneous p−n Junction Diode by Selective Doping of Few Layer $MoSe_2$ Using Ultraviolet Ozone for High-Performance Photovoltaic Devices. *Nanoscale* **2019**, *11*, 13469−13476.
(7) Zhang, K.; Zhang, T.; Cheng, G.; Li, T.; Wang, S.; Wei, W.; Zhou, X.; Yu, W.; Sun, Y.; Wang, P.; Zhang, D.; Zeng, C.; Wang, X.; Hu, W.; Fan, H. J.; Shen, G.; Chen, X.; Duan, X.; Chang, K.; Dai, N. Interlayer Transition and Infrared Photodetection in Atomically Thin Type-II $MoTe_2$/MoS_2 van Der Waals Heterostructures. *ACS Nano* **2016**, *10*, 3852−3858.
(8) Zhang, L.; Sharma, A.; Zhu, Y.; Zhang, Y.; Wang, B.; Dong, M.; Nguyen, H. T.; Wang, Z.; Wen, B.; Cao, Y.; Liu, B.; Sun, X.; Yang, J.; Li, Z.; Kar, A.; Shi, Y.; Macdonald, D.; Yu, Z.; Wang, X.; Lu, Y. Efficient and Layer-Dependent Exciton Pumping across Atomically Thin Organic-Inorganic Type-I Heterostructures. *Adv. Mater.* **2018**, *30*, 1803986.
(9) Yan, R.; Fathipour, S.; Han, Y.; Song, B.; Xiao, S.; Li, M.; Ma, N.; Protasenko, V.; Muller, D. A.; Jena, D.; Xing, H. G. Esaki Diodes in van Der Waals Heterojunctions with Broken-Gap Energy Band Alignment. *Nano Lett.* **2015**, *15*, 5791−5798.
(10) Qiu, X.; Yang, B.; Chen, H.; Liu, G.; Liu, Y.; Yuan, Y.; Huang, H.; Xie, H.; Niu, D.; Gao, Y.; Zhou, C. Efficient, Stable and Flexible Perovskite Solar Cells Using Two-Step Solution-Processed SnO_2 Layers as Electron-Transport-Material. *Org. Electron.* **2018**, *58*, 126−132.
(11) Yang, W. S.; Park, B.-W.; Jung, E. H.; Jeon, N. J.; Kim, Y. C.; Lee, D. U.; Shin, S. S.; Seo, J.; Kim, E. K.; Noh, J. H.; Seok, S. I. Iodide Management in Formamidinium-Lead-Halide−Based Perovskite Layers for Efficient Solar Cells. *Science* **2017**, *356*, 1376−1379.
(12) Wan, F.; Qiu, X.; Chen, H.; Liu, Y.; Xie, H.; Shi, J.; Huang, H.; Yuan, Y.; Gao, Y.; Zhou, C. Accelerated Electron Extraction and Improved UV Stability of TiO_2 Based Perovskite Solar Cells by SnO_2 Based Surface Passivation. *Org. Electron.* **2018**, *59*, 184−189.
(13) Tan, M.; Hu, C.; Lan, Y.; Khan, J.; Deng, H.; Yang, X.; Wang, P.; Yu, X.; Lai, J.; Song, H. 2D Lead Dihalides for High-Performance Ultraviolet Photodetectors and Their Detection Mechanism Investigation. *Small* **2017**, *13*, 1702024.
(14) Sun, L.; Wang, C.; Xu, L.; Wang, J.; Liu, X.; Chen, X.; Yi, G.-C. SbSI Whisker/PbI_2 Flake Mixed-Dimensional van Der Waals Heterostructure for Photodetection. *CrystEngComm* **2019**, *21*, 3779−3787.
(15) Zhang, J.; Huang, Y.; Tan, Z.; Li, T.; Zhang, Y.; Jia, K.; Lin, L.; Sun, L.; Chen, X.; Li, Z.; Tan, C.; Zhang, J.; Zheng, L.; Wu, Y.; Deng, B.; Chen, Z.; Liu, Z.; Peng, H. Low-Temperature Heteroepitaxy of 2D PbI_2/Graphene for Large-Area Flexible Photodetectors. *Adv. Mater.* **2018**, *30*, 1803194.
(16) Toulouse, A. S.; Isaacoff, B. P.; Shi, G.; Matuchova, M.; Kioupakis, E.; Merlin, R. Frenkel-like Wannier-Mott Excitons in Few Layer PbI_2. *Phys. Rev. B: Condens. Matter Mater. Phys.* **2015**, *91*, 165308.
(17) Sun, Y.; Zhou, Z.; Huang, Z.; Wu, J.; Zhou, L.; Cheng, Y.; Liu, J.; Zhu, C.; Yu, M.; Yu, P.; Zhu, W.; Liu, Y.; Zhou, J.; Liu, B.; Xie, H.; Cao, Y.; Li, H.; Wang, X.; Liu, K.; Wang, X.; Wang, J.; Wang, L.; Huang, W. Band Structure Engineering of Interfacial Semiconductors Based on Atomically Thin Lead Iodide Crystals. *Adv. Mater.* **2019**, *31*, 1806562.
(18) Xiao, J.; Liu, J.; Sun, K.; Zhao, Y.; Shao, Z.; Liu, X.; Yuan, Y.; Li, Y.; Xie, H.; Song, F.; Gao, Y.; Huang, H. PbI_2−MoS_2 Heterojunction: Van Der Waals Epitaxial Growth and Energy Band Alignment. *J. Phys. Chem. Lett.* **2019**, *10*, 4203−4208.
(19) Ma, Y.; Zhao, X.; Wang, T.; Li, W.; Wang, X.; Chang, S.; Li, Y.; Zhao, M.; Dai, X. Band Structure Engineering in a MoS_2/PbI_2 van Der Waals Heterostructure via an External Electric Field. *Phys. Chem. Chem. Phys.* **2016**, *18*, 28466−28473.
(20) Zheng, W.; Zheng, B.; Yan, C.; Liu, Y.; Sun, X.; Qi, Z.; Yang, T.; Jiang, Y.; Huang, W.; Fan, P.; Jiang, F.; Ji, W.; Wang, X.; Pan, A. Direct Vapor Growth of 2D Vertical Heterostructures with Tunable Band Alignments and Interfacial Charge Transfer Behaviors. *Adv. Sci.* **2019**, *6*, 1802204.
(21) Roy, A.; Movva, H. C. P.; Satpati, B.; Kim, K.; Dey, R.; Rai, A.; Pramanik, T.; Guchhait, S.; Tutuc, E.; Banerjee, S. K. Structural and Electrical Properties of $MoTe_2$ and $MoSe_2$ Grown by Molecular Beam Epitaxy. *ACS Appl. Mater. Interfaces* **2016**, *8*, 7396−7402.
(22) Rhyee, J.-S.; Kwon, J.; Dak, P.; Kim, J. H.; Kim, S. M.; Park, J.; Hong, Y. K.; Song, W. G.; Omkaram, I.; Alam, M. A.; Kim, S. High-Mobility Transistors Based on Large-Area and Highly Crystalline CVD-Grown $MoSe_2$ Films on Insulating Substrates. *Adv. Mater.* **2016**, *28*, 2316−2321.
(23) Chang, Y.-H.; Zhang, W.; Zhu, Y.; Han, Y.; Pu, J.; Chang, J.-K.; Hsu, W.-T.; Huang, J.-K.; Hsu, C.-L.; Chiu, M.-H.; Takenobu, T.; Li, H.; Wu, C.-I.; Chang, W.-H.; Wee, A. T. S.; Li, L.-J. Monolayer $MoSe_2$ Grown by Chemical Vapor Deposition for Fast Photodetection. *ACS Nano* **2014**, *8*, 8582−8590.
(24) He, X.; Zhang, L.; Chua, R.; Wong, P. K. J.; Arramel, A.; Feng, Y. P.; Wang, S. J.; Chi, D.; Yang, M.; Huang, Y. L.; Wee, A. T. S. Selective Self-Assembly of 2,3-Diaminophenazine Molecules on $MoSe_2$ Mirror Twin Boundaries. *Nat. Commun.* **2019**, *10*, 2847.
(25) Zhang, W.; Zhang, L.; Wong, P. K. J.; Yuan, J.; Vinai, G.; Torelli, P.; van der Laan, G.; Feng, Y. P.; Wee, A. T. S. Magnetic Transition in Monolayer VSe_2 *via* Interface Hybridization. *ACS Nano* **2019**, *13*, 8997−9004.
(26) Xie, Q.; Zheng, X.; Wu, D.; Chen, X.; Shi, J.; Han, X.; Zhang, X.; Peng, G.; Gao, Y.; Huang, H. High Electrical Conductivity of Individual Epitaxially Grown MoO_2 Nanorods. *Appl. Phys. Lett.* **2017**, *111*, 093505.
(27) Fang, L.; Chen, H.; Yuan, X.; Huang, H.; Chen, G.; Li, L.; Ding, J.; He, J.; Tao, S. Quick Optical Identification of the Defect Formation in Monolayer WSe_2 for Growth Optimization. *Nanoscale Res. Lett.* **2019**, *14*, 274.
(28) Tian, G.; Shen, Y.; He, B.; Yu, Z.; Song, F.; Lu, Y.; Wang, P.; Gao, Y.; Huang, H. Effects of Monolayer Bi on the Self-Assembly of DBBA on Au(111). *Surf. Sci.* **2017**, *665*, 89−95.
(29) He, B.; Tian, G.; Gou, J.; Liu, B.; Shen, K.; Tian, Q.; Yu, Z.; Song, F.; Xie, H.; Gao, Y.; Lu, Y.; Wu, K.; Chen, L.; Huang, H. Structural and Electronic Properties of Atomically Thin Bismuth on Au(111). *Surf. Sci.* **2019**, *679*, 147−153.
(30) Tian, Q.; He, B.; Zhao, Y.; Wang, S.; Xiao, J.; Song, F.; Wang, Y.; Lu, Y.; Xie, H.; Huang, H.; Gao, Y. Electronic Structure Evolution at DBBA/Au(111) Interface W/O Bismuth Insertion Layer. *Synth. Met.* **2019**, *251*, 24−29.
(31) Wu, D.; Shi, J.; Zheng, X.; Liu, J.; Dou, W.; Gao, Y.; Yuan, X.; Ouyang, F.; Huang, H. CVD Grown MoS_2 Nanoribbons on MoS_2 Covered Sapphire(0001) Without Catalysts. *Phys. Status Solidi RRL* **2019**, *13*, 1900063.
(32) Shi, J.; Wu, D.; Zheng, X.; Xie, D.; Song, F.; Zhang, X.; Jiang, J.; Yuan, X.; Gao, Y.; Huang, H. From MoO_2 @ MoS_2 Core-Shell Nanorods to MoS_2 Nanobelts. *Phys. Status Solidi B* **2018**, *255*, 1800254.
(33) Kresse, G.; Furthmüller, J. Efficient Iterative Schemes for *Ab Initio* Total-Energy Calculations Using a Plane-Wave Basis Set. *Phys. Rev. B: Condens. Matter Mater. Phys.* **1996**, *54*, 11169−11186.
(34) Kresse, G.; Hafner, J. *Ab Initio* Molecular Dynamics for Liquid Metals. *Phys. Rev. B: Condens. Matter Mater. Phys.* **1993**, *47*, 558−561.
(35) Blöchl, P. E. Projector Augmented-Wave Method. *Phys. Rev. B: Condens. Matter Mater. Phys.* **1994**, *50*, 17953−17979.

https://dx.doi.org/10.1021/acsami.0c04985
ACS Appl. Mater. Interfaces 2020, 12, 32099−32105

(36) Perdew, J. P.; Burke, K.; Ernzerhof, M. Generalized Gradient Approximation Made Simple [Phys. Rev. Lett. 77, 3865 (1996)]. *Phys. Rev. Lett.* **1997**, *78*, 1396.

(37) Di Sante, D.; Stroppa, A.; Barone, P.; Whangbo, M. H.; Picozzi, S. Emergence of Ferroelectricity and Spin-Valley Properties in Two-Dimensional Honeycomb Binary Compounds. *Phys. Rev. B: Condens. Matter Mater. Phys.* **2015**, *91*, 161401.

(38) Liu, H. J.; Jiao, L.; Xie, L.; Yang, F.; Chen, J. L.; Ho, W. K.; Gao, C. L.; Jia, J. F.; Cui, X. D.; Xie, M. H. Molecular-Beam Epitaxy of Monolayer and Bilayer WSe_2 : A Scanning Tunneling Microscopy/Spectroscopy Study and Deduction of Exciton Binding Energy. *2D Mater.* **2015**, *2*, 034004.

(39) Barja, S.; Wickenburg, S.; Liu, Z.-F.; Zhang, Y.; Ryu, H.; Ugeda, M. M.; Hussain, Z.; Shen, Z.-X.; Mo, S.-K.; Wong, E.; Salmeron, M. B.; Wang, F.; Crommie, M. F.; Ogletree, D. F.; Neaton, J. B.; Weber-Bargioni, A. Charge Density Wave Order in 1D Mirror Twin Boundaries of Single-Layer $MoSe_2$. *Nat. Phys.* **2016**, *12*, 751−756.

(40) Zhang, C.; Chen, Y.; Johnson, A.; Li, M.-Y.; Li, L.-J.; Mende, P. C.; Feenstra, R. M.; Shih, C.-K. Probing Critical Point Energies of Transition Metal Dichalcogenides: Surprising Indirect Gap of Single Layer WSe_2. *Nano Lett.* **2015**, *15*, 6494−6500.

(41) Ugeda, M. M.; Bradley, A. J.; Shi, S.-F.; da Jornada, F. H.; Zhang, Y.; Qiu, D. Y.; Ruan, W.; Mo, S.-K.; Hussain, Z.; Shen, Z.-X.; Wang, F.; Louie, S. G.; Crommie, M. F. Giant Bandgap Renormalization and Excitonic Effects in a Monolayer Transition Metal Dichalcogenide Semiconductor. *Nat. Mater.* **2014**, *13*, 1091−1095.

(42) Hor, Y. S.; Richardella, A.; Roushan, P.; Xia, Y.; Checkelsky, J. G.; Yazdani, A.; Hasan, M. Z.; Ong, N. P.; Cava, R. J. P-Type Bi_2Se_3 for Topological Insulator and Low-Temperature Thermoelectric Applications. *Phys. Rev. B: Condens. Matter Mater. Phys.* **2009**, *79*, 195208.

(43) Wang, H.; Kong, D.; Johanes, P.; Cha, J. J.; Zheng, G.; Yan, K.; Liu, N.; Cui, Y. $MoSe_2$ and WSe_2 Nanofilms with Vertically Aligned Molecular Layers on Curved and Rough Surfaces. *Nano Lett.* **2013**, *13*, 3426−3433.

(44) Dai, T.; Liu, Y.; Liu, X.; Xie, D.; Li, Y. High Performance Photodetectors Constructed on Atomically Thin Few-Layer $MoSe_2$ Synthesized Using Atomic Layer Deposition and a Chemical Vapor Deposition Chamber. *J. Alloys Compd.* **2019**, *785*, 951−957.

(45) Zhang, X.; Qiao, X.-F.; Shi, W.; Wu, J.-B.; Jiang, D.-S.; Tan, P.-H. Phonon and Raman scattering of two-dimensional transition metal dichalcogenides from monolayer, multilayer to bulk material. *Chem. Soc. Rev.* **2015**, *44*, 2757.

(46) Molina-Sánchez, A.; Wirtz, L. Phonons in Single-Layer and Few-Layer MoS_2 and WS_2. *Phys. Rev. B: Condens. Matter Mater. Phys.* **2011**, *84*, 155413.

(47) Lee, C.; Yan, H.; Brus, L. E.; Heinz, T. F.; Hone, J.; Ryu, S. Anomalous Lattice Vibrations of Single- and Few-Layer MoS_2. *ACS Nano* **2010**, *4*, 2695−2700.

(48) Zhao, W.; Ghorannevis, Z.; Amara, K. K.; Pang, J. R.; Toh, M.; Zhang, X.; Kloc, C.; Tan, P. H.; Eda, G. Lattice Dynamics in Monoand Few-Layer Sheets of WS_2 and WSe_2. *Nanoscale* **2013**, *5*, 9677−9683.

(49) Zhou, X.; Zhou, N.; Li, C.; Song, H.; Zhang, Q.; Hu, X.; Gan, L.; Li, H.; Lü, J.; Luo, J.; Xiong, J.; Zhai, T. Vertical Heterostructures based on $SnSe_2/MoS_2$ for High Performance Photodetectors. *2D Mater* **2017**, *4*, 025048.

(50) Li, H.; Wu, J.-B.; Ran, F.; Lin, M.-L.; Liu, X.-L.; Zhao, Y.; Lu, X.; Xiong, Q.; Zhang, J.; Huang, W.; Zhang, H.; Tan, P.-H. Interfacial Interactions in van der Waals Heterostructures of MoS_2 and Graphene. *ACS Nano* **2017**, *11*, 11714.

(51) Zhang, Z.; Zheng, W.; Wang, W.; Zhong, D.; Huang, F. Anisotropic Temperature-Dependence of Optical Phonons in Layered PbI_2. *J. Raman Spectrosc.* **2018**, *49*, 775−779.

(52) Wang, Y.; Zhang, S.; Di Huang; Cheng, J.; Li, Y.; Wu, S. Screening Effect of Graphite and Bilayer Graphene on Excitons in $MoSe_2$ Monolayer. *2D Mater.* **2016**, *4*, 015021.

(53) Xu, L.; Zhao, L.; Wang, Y.; Zou, M.; Zhang, Q.; Cao, A. Analysis of Photoluminescence Behavior of High-Quality Single-Layer MoS_2. *Nano Res.* **2019**, *12*, 1619−1624.

(54) Carozo, V.; Wang, Y.; Fujisawa, K.; Carvalho, B. R.; McCreary, A.; Feng, S.; Lin, Z.; Zhou, C.; Perea-López, N.; Elías, A. L.; Kabius, B.; Crespi, V. H.; Terrones, M. Optical Identification of Sulfur Vacancies: Bound Excitons at the Edges of Monolayer Tungsten Disulfide. *Sci. Adv.* **2017**, *3*, No. e1602813.

(55) O'Donnell, K. P.; Chen, X. Temperature Dependence of Semiconductor Band Gaps. *Appl. Phys. Lett.* **1991**, *58*, 2924−2926.

(56) Li, D.; Xiao, Z.; Golgir, H. R.; Jiang, L.; Singh, V. R.; Keramatnejad, K.; Smith, K. E.; Hong, X.; Jiang, L.; Silvain, J.-F.; Lu, Y. Large-Area 2D/3D MoS_2-MoO_2 Heterostructures with Thermally Stable Exciton and Intriguing Electrical Transport Behaviors. *Adv. Electron. Mater.* **2017**, *3*, 1600335.

https://dx.doi.org/10.1021/acsami.0c04985
ACS Appl. Mater. Interfaces 2020, 12, 32099−32105